
DATA-DRIVEN PROTECTION LEVELS FOR CAMERA AND 3D MAP-BASED SAFE URBAN LOCALIZATION

Shubh Gupta

Department of Electrical Engineering
Stanford University
Stanford, CA 94305
shubhgup@stanford.edu

Grace X. Gao

Department of Aeronautics & Astronautics
Stanford University
Stanford, CA 94305
gracegao@stanford.edu

December 23, 2024

ABSTRACT

Reliably assessing the error in an estimated vehicle position is integral for ensuring the vehicle's safety in urban environments. Many existing approaches use GNSS measurements to characterize protection levels (PLs) as probabilistic upper bounds on the position error. However, GNSS signals might be reflected or blocked in urban environments, and thus additional sensor modalities need to be considered to determine PLs. In this paper, we propose a novel approach for computing PLs by matching camera image measurements to a LiDAR-based 3D map of the environment. We specify a Gaussian mixture model probability distribution of position error using deep neural network-based data-driven models and statistical outlier weighting techniques. From the probability distribution, we compute the PLs by evaluating the position error bound using numerical line-search methods. Through experimental validation with real-world data, we demonstrate that the PLs computed from our method are reliable bounds on the position error in urban environments.

1 Introduction

In recent years, research on autonomous navigation for urban environments has been garnering increasing attention. Many publications have targeted different aspects of navigation such as route planning, perception and localization [1, 2, 3, 4]. For trustworthy operation in each of these aspects, assessing the level of safety of the vehicle from potential system failures is critical. However, fewer works have examined the problem of safety quantification for autonomous vehicles.

In the context of satellite-based localization, safety is typically addressed via integrity monitoring (IM) [5]. Within IM, protection levels specify a statistical upper bound on the error in an estimated position of the vehicle, which can be trusted to enclose the position errors with a required probabilistic guarantee. Various methods [6, 7, 8] have been proposed over the years for computing protection levels. However, most of these approaches focus on GNSS-only navigation. These approaches do not directly apply to GNSS-denied urban environments, where visual sensors are becoming increasingly preferred [9]. Although various options in visual sensors exist in the market, camera sensors are inexpensive, lightweight, and have been widely employed in industry. For quantifying localization safety in GNSS-denied urban environments, there is thus a need to develop new ways of computing protection levels using camera image measurements.

Since protection levels are bounds over the position error, computing them from camera image measurements requires a model that relates the measurements to position error in the estimate of the vehicle location. However, characterizing such a model is not straightforward. This is because the relation between a vehicle location in an environment and the corresponding camera image measurement is complex which depends on identifying and matching structural patterns in the measurements with prior known information about the environment [10, 1, 2, 11].

Recently, data-driven techniques based on deep neural networks (DNNs) have demonstrated state-of-the-art performance in determining the state of the camera sensor, comprising of its position and orientation, by identifying and matching

patterns in images with a known map of the environment [12, 13, 14, 15] or an existing database of images [16, 17]. By leveraging datasets consisting of multiple images with known camera states in an environment, these approaches train a DNN to model the relationship between an image and the corresponding state. However, the model characterized by the DNN can often be erroneous or brittle. For instance, recent research has shown that the output of a DNN can change significantly with minimal changes to the inputs [18]. Thus, for using DNNs to determine the position error, uncertainty in the output of the DNN must also be addressed.

DNN-based algorithms consider two types of uncertainty [19, 20]. *Aleatoric* uncertainty results from the noise present in the inputs to the DNN, due to which a precise output cannot be produced. For camera image inputs, sources of noise include illumination changes, occlusion or the presence of visually ambiguous structures, such as windows tessellated along a wall [19]. On the other hand, *epistemic* uncertainty exists within the model itself. Sources of epistemic uncertainty include poorly determined DNN model parameters as well as external factors that are not considered in the model [21], such as environmental features that might be ignored by the algorithm while matching the camera images to the environment map.

While aleatoric uncertainty is typically modeled as the input-dependent variance in the output of the DNN [19, 22, 23], epistemic uncertainty relates to the DNN model and, therefore, requires further deliberation. Existing approaches approximate epistemic uncertainty by assuming a probability distribution over the weight parameters of the DNN to represent the ignorance about the correct parameters [24, 25, 26]. However, these approaches assume that a correct value of the parameters exists and that the probability distribution over the weight parameters captures the uncertainty in the model, both of which do not necessarily hold in practice [27]. This inability of existing DNN-based methods to properly characterize uncertainty limits their applicability to safety-critical applications, such as localization of autonomous vehicles.

In this paper, we propose a novel method for computing protection levels associated with a given vehicular state estimate (position and orientation) from camera image measurements and a 3D map of the environment. This work is based on our recent ION GNSS+ 2020 conference paper [28] and includes additional experiments and improvements to the DNN training process. Recently, high-definition 3D environment maps in the form of LiDAR point clouds have become increasingly available through industry players such as HERE, TomTom, Waymo and NVIDIA, as well as through projects such as USGS 3DEP [29] and OpenTopography [30]. Furthermore, LiDAR-based 3D maps are more robust to noise from environmental factors, such as illumination and weather, than image-based maps [31]. Hence, we use LiDAR-based 3D maps in our approach.

Previously, CMRNet [14] has been proposed as a DNN-based approach for determining the vehicular state from camera images and a LiDAR-based 3D map. In our approach, we extend the DNN architecture proposed in [14] to model the position error and variance (aleatoric uncertainty) in the vehicular state estimate. To assess the epistemic uncertainty in the position error, we evaluate the DNN position error outputs at multiple candidate states in the vicinity of the state estimate, and combine the outputs into samples of the state estimate position error. Fig. 1 shows the architecture of our proposed approach. Given a state estimate, we first select multiple candidate states from its neighborhood. Using the DNN, we then evaluate the position error and variance for each candidate state by comparing the camera image measurement with a local map constructed from the candidate state and the 3D environment map. Next, we linearly combine the position error outputs from the DNN with the relative positions of candidate states into samples of the state estimate position error. We then weight these samples to mitigate the impact of outliers and project them to the error direction into samples of the position error magnitude. Subsequently, we combine the position error magnitude samples, outlier weights, and variance evaluated from the DNN to construct a Gaussian mixture model probability distribution of the position error, and numerically evaluate its intervals to compute protection levels.

Our main contributions are as follows:

1. We extend the CMRNet [14] architecture to model both the position error in the vehicular state estimate as well as variance in the DNN output. Using the 3D LiDAR-based map of the environment, we first construct a local map representation with respect to the vehicular state estimate. Then, we use the DNN to analyze the correspondence between the camera image measurement and the local map for determining position error and variance.
2. We develop a novel method for capturing epistemic uncertainty in the DNN position error output. Unlike existing approaches which assume a probability distribution over DNN weight parameters, we directly analyze different position errors that are determined by the DNN for multiple candidate states selected from within a neighborhood of the state estimate. The position error outputs from the DNN corresponding to the candidate states are then linearly combined with the candidate states' relative position from the state estimate, to obtain an empirical distribution of the state estimate position error.

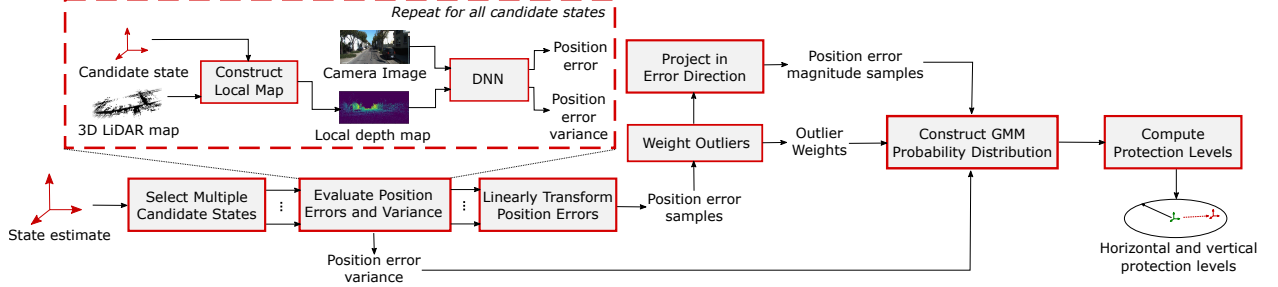


Figure 1: Architecture of our proposed approach for computing protection levels. Given a state estimate, multiple candidate states are selected from its neighborhood and the corresponding position error and variance for each candidate state are evaluated using the DNN. The position errors are linearly combined with the relative position of the candidate states to obtain samples of the state estimate position error, which are then weighted to determine outliers and are projected into samples of the position error magnitude. Finally, the position error magnitude samples, outlier weights and variance evaluated from the DNN are combined to construct a Gaussian Mixture Model probability distribution, from which the horizontal and vertical protection levels are computed through numerical evaluation of its probability intervals.

3. We design an outlier weighting scheme to account for possible errors in the DNN output at inputs that differ from the training data. Our approach weighs the position error samples from the empirical distribution using a robust outlier detection metric, known as robust Z-score [32], along x , y and z axes individually. The weighted position error samples in each dimension are then combined into samples of the position error magnitude in the horizontal and vertical dimensions.
4. We construct the horizontal and vertical protection levels as intervals over the probability distribution of the position error magnitude. We model this probability distribution as a Gaussian Mixture Model [33] from the position error magnitude samples, DNN variance and outlier weights.
5. We demonstrate the applicability of our approach in urban environments, by experimentally validating the protection levels computed from our method on real-world data with multiple camera images and different state estimates.

The remainder of this paper is structured as follows: Section II discusses related work. Section III formulates the problem of estimating protection levels. Section IV describes the two types of uncertainties considered in our approach. Section V details our algorithm. Section VI presents the results from experimentation with real-world data. We conclude the paper in Section VII.

2 Related Work

Several methods have been developed over the years which characterize protection levels in the context of GNSS-based urban navigation. Jiang and Wang [6] compute horizontal protection levels using an iterative search-based method and test statistic based on the bivariate normal distribution. Azaola *et al.* [7] develop a method which utilizes the isotropy of residual vectors from the least-squares position estimation to compute the protection levels. Tran and Presti [8] combine Advanced Receiver Autonomous Integrity Monitoring (ARAIM) with Kalman filtering, and compute the protection levels by considering the set of position solutions which arise after excluding faulty measurements. These approaches compute the protection levels by deriving the mathematical relation between measurement and position domain errors. However, such a relation is difficult to formulate with camera image measurements and a 3D map, since the position error in this case depends on various factors such as the structure of buildings in the environment, available visual features and illumination levels. Therefore, our proposed approach uses deep learning to approximate the complex relation between the camera image measurements, 3D map and position errors.

Deep learning has been widely applied for determining position information from camera images. Kendall *et al.* [34] train a DNN using images from a single environment to learn a relation between the image and the camera 6-DOF pose. Taira *et al.* [17] learn image features using a DNN and apply feature extraction and matching techniques to estimate the 6-DOF camera pose relative to a known 3D map of the environment. Sarlin *et al.* [16] develop a deep learning-based 2D-3D matching technique to obtain 6-DOF camera pose from images and a 3D environment model. However, these approaches do not model the corresponding uncertainty associated with the estimated camera pose, or account for failures in DNN approximation [18], which is necessary for characterizing safety measures such as protection levels.

Some recent works have proposed to estimate the uncertainty associated with deep learning algorithms. Kendall and Cipolla [24] estimate the uncertainty in DNN-based camera pose estimation from images, by evaluating the network multiple times through dropout [25]. Loquercio *et al.* [20] propose a general framework for estimating uncertainty in deep learning as variance computed from both aleatoric and epistemic sources. McAllister *et al.* [22] suggest using Bayesian deep learning to determine uncertainty and quantify safety in autonomous vehicles, by placing probability distributions over DNN weights to represent the uncertainty in the DNN model. Yang *et al.* [23] jointly estimate the vehicle odometry, scene depth and uncertainty from sequential camera images. However, the uncertainty estimates from these algorithms do not take into account the inaccuracy of the trained DNN model, or the influence of the underlying environment structure on the DNN outputs. In our approach, we evaluate the DNN position error outputs at inputs corresponding to multiple states in the environment, and utilize these position errors for characterizing uncertainty both from inaccuracy in the DNN model as well as from the environment structure around the state estimate.

To the best of our knowledge, our approach is the first that applies data-driven algorithms for computing protection levels by characterizing the uncertainty from different error sources. The proposed method seeks to leverage the high-fidelity function modeling capability of DNNs and combine it with techniques from robust statistics and integrity monitoring to compute robust protection levels using camera image measurements and 3D map of the environment.

3 Problem Formulation

We consider the scenario of a vehicle navigating in an urban environment using measurements acquired by an on-board camera. The 3D LiDAR map of the environment \mathcal{M} that consists of points $\mathbf{p} \in \mathbb{R}^3$ is assumed to be pre-known from either openly available repositories [29, 30] or from Simultaneous Localization and Mapping algorithms [35].

The vehicular state $\mathbf{s}_t = [\mathbf{x}_t, \mathbf{r}_t]$ at time t is a 6-element vector comprising of its 3D position $\mathbf{x}_t = [x_t, y_t, z_t]$ along x, y and z -dimensions and 3D orientation $\mathbf{o}_t = [\phi_t, \theta_t, \psi_t]$ corresponding to roll, pitch and yaw dimensions, respectively. The vehicle state estimates over time are denoted as $\{\mathbf{s}_t\}_{t=1}^{T_{\max}}$ where T_{\max} denotes the total time in a navigation sequence. At each time t , the vehicle captures an RGB camera image $I_t \in \mathbb{R}^{l \times w \times 3}$ from the on-board camera, where l and w denote pixels along length and width dimensions, respectively.

Given an integrity risk specification IR , our objective is to compute the horizontal protection level $PL_{h,t}$ and vertical protection levels $PL_{v,t}$ at time t , which denote the maximal bounds on the position error magnitude with a probabilistic guarantee of at least $1 - IR$. Formally,

$$PL_{h,t} = \sup \left\{ \rho \mid \mathbb{P} \left(\sqrt{(x_t - x_t^*)^2 + (y_t - y_t^*)^2} \leq \rho \right) \geq 1 - IR \right\}$$

$$PL_{v,t} = \sup \left\{ \rho \mid \mathbb{P} (|z_t - z_t^*| \leq \rho) \geq 1 - IR \right\},$$

where $\mathbf{x}_t^* = [x_t^*, y_t^*, z_t^*]$ denotes the unknown true vehicle position at time t .

4 Types of Uncertainty in Position Error

Protection levels for a state estimate \mathbf{s}_t at time t depend on the uncertainty in determining the associated position error $\Delta \mathbf{x}_t = [\Delta x_t, \Delta y_t, \Delta z_t]$ between the state estimate position \mathbf{x}_t and the true position \mathbf{x}_t^* from the camera image I_t and the environment map \mathcal{M} . We consider two different kinds of uncertainty, which are categorized by the source of inaccuracy in determining the position error $\Delta \mathbf{x}_t$: aleatoric and epistemic uncertainty.

4.1 Aleatoric Uncertainty

Aleatoric uncertainty refers to the uncertainty from noise present in the camera image measurements I_t and the environment map \mathcal{M} , due to which a precise value of the position error $\Delta \mathbf{x}_t$ cannot be determined. Similar to existing approaches [19, 22, 23], we characterize the aleatoric uncertainty by using a DNN to model the variance $\sigma_t^2 = [\sigma_{x,t}^2, \sigma_{y,t}^2, \sigma_{z,t}^2]$ in the position error $\Delta \mathbf{x}_t$.

Aleatoric uncertainty by itself does not accurately represent the uncertainty in determining the position error. This is because aleatoric uncertainty assumes that the noise present in training data also represents the noise in all future inputs and that the DNN approximation is error-free. These assumptions fail in scenarios when the input at evaluation time is different from the training data or when the input contains features that occur rarely in the real world [18]. Thus, relying purely on aleatoric uncertainty can lead to an overconfident estimates of the position error uncertainty [19].

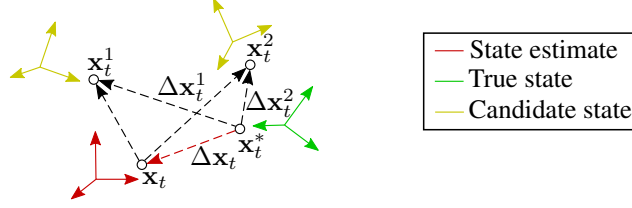


Figure 2: Position error $\Delta \mathbf{x}_t$ in the state estimate position \mathbf{x}_t is a linear combination of the position error $\Delta \mathbf{x}_t^i$ in position \mathbf{x}_t^i of any candidate state s_t^i and the relative position vector between \mathbf{x}_t^i and \mathbf{x}_t .

4.2 Epistemic Uncertainty

Epistemic uncertainty relates to the inaccuracies in the model for determining the position error $\Delta \mathbf{x}_t$. In our approach, we characterize the epistemic uncertainty by leveraging a geometrical property of the position error $\Delta \mathbf{x}_t$, where for the same camera image I_t , $\Delta \mathbf{x}_t$ can be obtained by linearly combining the position error $\Delta \mathbf{x}_t^i$ computed for any *candidate state* s_t^i and the relative position of s_t^i from the state estimate s_t (Fig. 2). Hence, using known relative positions and orientations of N_C candidate states $\{s_t^1, \dots, s_t^{N_C}\}$ from s_t , we transform the different position errors $\{\Delta \mathbf{x}_t^1, \dots, \Delta \mathbf{x}_t^{N_C}\}$ determined for the candidate states into samples of the state estimate position error $\Delta \mathbf{x}_t$. The empirical distribution comprised of these position error samples characterizes the epistemic uncertainty in the position error estimated using the DNN.

5 Data-Driven Protection Levels

This section details our algorithm for computing data-driven protection levels for the state estimate s_t at time t , using the camera image I_t and environment map \mathcal{M} . The architecture of our approach is illustrated in Fig. 1. First, we describe the method for generating local representations of the 3D environment map \mathcal{M} with respect to the state estimate s_t . Then, we illustrate the architecture of the DNN. Next, we discuss the loss functions and optimization procedures using in DNN training. We then detail the method for selecting multiple candidate states from the neighborhood of the state estimate s_t . Using position errors and variance evaluated from the DNN for each of these candidate states, we then illustrate the process for transforming the candidate state position errors into multiple samples of the state estimate position error. Then, to mitigate the impact of outliers in the computed position error samples, we detail the procedure for computing outlier weights associated with each position error sample. Using these outlier weights, we then describe the method for computing the error direction and obtaining samples of position error magnitude. Next, we characterize the probability distribution over position error magnitudes in both horizontal and vertical directions. Finally, we detail the approach for determining protection levels from the probability distribution by numerical methods.

5.1 Local Map Representation

A local representation of the 3D LiDAR map of the environment captures the environment information in the vicinity of the state estimate s_t at time t . By comparing the environment information captured in the local map with the camera image $I_t \in \mathbb{R}^{l \times w \times 3}$ using a DNN, we estimate the position error $\Delta \mathbf{x}_t$ and variance σ_t^2 in the state estimate s_t . For computing the local maps, we utilize the LiDAR-image generation procedure described in [14]. Similar to their approach, we generate the local map $L(s, \mathcal{M}) \in \mathbb{R}^{l \times w}$ associated with a vehicle state s and LiDAR environment map \mathcal{M} in two steps.

1. First, we determine the rigid-body transformation matrix H_s in the special Euclidean group $SE(3)$ corresponding to the vehicle state s ,

$$H_s = \begin{bmatrix} R_s & T_s \\ \mathbf{0}_{1 \times 3} & 1 \end{bmatrix} \in SE(3), \quad (1)$$

where

- R_s denotes the rotation matrix corresponding to the orientation elements $\mathbf{o} = [\phi, \theta, \psi]$ in the state s
- T_s denotes the translation vector corresponding to the position elements $\mathbf{x} = [x, y, z]$ in the state s .

Using the matrix H_s , we rotate and translate the points in the map \mathcal{M} to the map \mathcal{M}_s in the reference frame of the state s ,

$$\mathcal{M}_s = \{[I_{3 \times 3} \quad \mathbf{0}_{3 \times 1}] \cdot H_s \cdot [\mathbf{p}^\top \quad 1]^\top \mid \mathbf{p} \in \mathcal{M}\}, \quad (2)$$

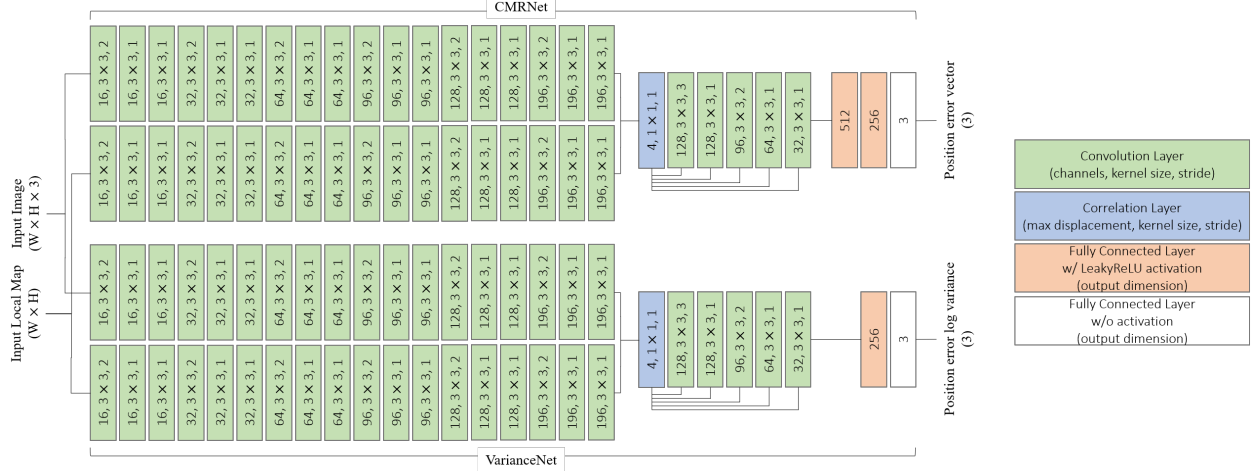


Figure 3: Architecture of our deep neural network for estimating both position error and variance. The position error is determined using CMRNet [14], and employs correlation layers [37] for comparing feature representations of the camera image and the local depth map. Using a similar architecture, we design VarianceNet which produces logarithm of the variance in the position error output.

where I denotes the identity matrix.

For maintaining computational efficiency in the case of large maps, we use the points in the LiDAR map \mathcal{M}_s that lie in a sub-region around the state s , as well as in the direction of the vehicle orientation.

2. In the second step, we apply the occlusion estimation filter presented in [36] to identify and remove occluded points along rays from the camera center. For each pair of points $(\mathbf{p}^{(i)}, \mathbf{p}^{(j)})$ where $\mathbf{p}^{(i)}$ is closer to the state s , $\mathbf{p}^{(j)}$ is marked occluded if the angle between the ray from $\mathbf{p}^{(j)}$ to the camera center and the line from $\mathbf{p}^{(j)}$ to $\mathbf{p}^{(i)}$ is less than a threshold. Then, the remaining points are projected to the camera image frame using the camera projection matrix K to generate the local depth map $L(s, \mathcal{M})$. The i th point $\mathbf{p}^{(i)}$ in \mathcal{M}_s is projected as,

$$\begin{aligned} [p_x \quad p_y \quad c]^\top &= K \cdot \mathbf{p}^{(i)} \\ [L(s, \mathcal{M})]_{([p_x/c], [p_y/c])} &= [0 \quad 0 \quad 1] \cdot \mathbf{p}^{(i)}, \end{aligned}$$

where

- p_x, p_y denote the projected 2D coordinates with scaling term c
- $[L(s, \mathcal{M})]_{(p_x, p_y)}$ denotes the (p_x, p_y) pixel position in the local map $L(s, \mathcal{M})$.

The local depth map $L(s, \mathcal{M})$ for state s visualizes the environment features that are expected to be captured in a camera image obtained from the state s . However, the obtained camera image I_t is associated with the true state \mathbf{s}_t^* that might be different from the state estimate \mathbf{s}_t . Nevertheless, for reasonably small position and orientation differences between the state estimate \mathbf{s}_t and true state \mathbf{s}_t^* , the local map $L(s, \mathcal{M})$ contains features that correspond with some of the features in the camera image I_t that we use to estimate the position error.

5.2 DNN Architecture

We use a DNN to estimate the position error $\Delta \mathbf{x}_t$ and its variance σ_t^2 by implicitly identifying and comparing the positions of corresponding features in camera image I_t and the local depth map $L(\mathbf{s}_t, \mathcal{M})$ associated with the state estimate \mathbf{s}_t .

The architecture of our DNN is given in Fig. 3. Our DNN comprises of two separate modules, one for estimating the position error $\Delta \mathbf{x}_t$ and other for the variance σ_t^2 . The first module for estimating the position error $\Delta \mathbf{x}_t$ is based on CMRNet [14]. CMRNet was originally proposed as an algorithm to iteratively determine the position and orientation of a vehicle using a camera image and 3D LiDAR map, starting from a provided initial state. For determining position error $\Delta \mathbf{x}_t$ using CMRNet, we use the state estimate \mathbf{s}_t as the provided initial state and the corresponding DNN output for translating the state \mathbf{s}_t as the position error $\Delta \mathbf{x}_t$. Formally, given a vehicle state s and camera image I_t at time t , the

approximated position error $\Delta\mathbf{x}$ and orientation error $\Delta\mathbf{r}$ are expressed as,

$$\Delta\mathbf{s}, \Delta\mathbf{r} = \text{CMRNet}(I_t, L(\mathbf{s}, \mathcal{M})). \quad (3)$$

Note that CMRNet also estimates the orientation error $\Delta\mathbf{r}$ as a unit quaternion. However, we discard it at evaluation time since the protection levels only depend on the position error. Additionally, the original CMRNet architecture estimates corrections to the vehicle position and orientation in the frame of reference of the state \mathbf{s} itself. Since the protection levels are defined in the reference frame from which the camera image I_t is captured, we simply transform the determined position error $\Delta\mathbf{x}$ to this reference frame by rotating it with $(\Delta\mathbf{r})^{-1}$ before discarding the rotation output. For brevity, we will refer to this position error output in the camera image reference frame as $\Delta\mathbf{x}$.

For approximating the variance σ_t^2 associated with the position error output, our second DNN module (referred to as VarianceNet) uses a similar network structure as CMRNet, but with 256 and 3 artificial neurons in the last two fully connected layers to prevent overfitting. For stable training, VarianceNet produces logarithm of the variance as output, represented as $\log \sigma_t^2$, which is converted to the variance by then taking the exponent. Formally, given a vehicle state \mathbf{s} and camera image I_t at time t , the log variance $\log \sigma^2$ is approximated as,

$$\log \sigma^2 = \text{VarianceNet}(I_t, L(\mathbf{s}, \mathcal{M})). \quad (4)$$

The feature extraction modules in VarianceNet and CMRNet are separate since the two tasks are complementary: for estimating position error, the DNN must learn features that are robust to noise in the inputs while the variance in the estimated position error depends on the noise itself.

5.3 Loss Functions

The loss function for training the DNN must penalize position error outputs that differ from the corresponding ground truth present in the dataset, as well as penalize variance that overestimates or underestimates the uncertainty in the position error predictions. Furthermore, the loss must incentivize the DNN to extract useful features from the camera image and local map inputs for predicting the position error. Hence, we consider three additive components in our loss function $\mathcal{L}(\cdot)$,

$$\mathcal{L}(\Delta\mathbf{x}^*, \Delta\mathbf{x}, \log \sigma^2) = \alpha_{\text{Huber}} \mathcal{L}_{\text{Huber}}(\Delta\mathbf{x}^*, \Delta\mathbf{x}) + \alpha_{\text{MLE}} \mathcal{L}_{\text{MLE}}(\Delta\mathbf{x}^*, \Delta\mathbf{x}, \log \sigma^2) + \alpha_{\text{Ang}} \mathcal{L}_{\text{Ang}}(\Delta\mathbf{r}^*, \Delta\mathbf{r}), \quad (5)$$

where

- $\Delta\mathbf{x}^*, \Delta\mathbf{r}^*$ denotes the vector-valued position and orientation error in the state estimate \mathbf{s} with respect to the unknown true state \mathbf{s}^*
- $\mathcal{L}_{\text{Huber}}(\cdot)$ denotes the Huber loss function [38]
- $\mathcal{L}_{\text{MLE}}(\cdot)$ denotes the loss function for the maximum likelihood estimation of position error $\Delta\mathbf{x}$ and log variance $\log \sigma^2$
- $\mathcal{L}_{\text{Ang}}(\cdot)$ denotes the quaternion angular distance from [14]
- $\alpha_{\text{Huber}}, \alpha_{\text{MLE}}, \alpha_{\text{Ang}}$ are coefficients for weighting each loss term.

We employ the Huber loss $\mathcal{L}_{\text{Huber}}(\cdot)$ and quaternion angular distance $\mathcal{L}_{\text{Ang}}(\cdot)$ terms from [14]. The Huber loss term $\mathcal{L}_{\text{Huber}}(\cdot)$ penalizes the position error output $\Delta\mathbf{x}$ of the DNN,

$$\begin{aligned} \mathcal{L}_{\text{Huber}}(\Delta\mathbf{x}^*, \Delta\mathbf{x}) &= \sum_{X=x,y,z} D_{\text{Huber}}(\Delta X^*, \Delta X) \\ D_{\text{Huber}}(a^*, a) &= \begin{cases} \frac{1}{2}(a - a^*)^2 & \text{for } |a - a^*| \leq \delta \\ \delta \cdot (|a - a^*| - \frac{1}{2}\delta) & \text{otherwise} \end{cases}, \end{aligned}$$

where δ is a hyperparameter for adjusting the penalty assignment to small error values. In this paper, we set $\delta = 1$. Unlike the more common mean squared error, the penalty assigned to higher error values is linear in Huber loss instead of quadratic. Thus, Huber loss is more robust to outliers and leads to more stable training as compared with squared error. The quaternion angular distance term $\mathcal{L}_{\text{Ang}}(\cdot)$ penalizes the orientation error output $\Delta\mathbf{r}$ from CMRNet,

$$\begin{aligned} \mathcal{L}_{\text{Ang}}(\Delta\mathbf{r}^*, \Delta\mathbf{r}) &= D_{\text{Ang}}(\Delta\mathbf{r}^* \times \Delta\mathbf{r}^{-1}) \\ D_{\text{Ang}}(\mathbf{q}) &= \text{atan2} \left(\sqrt{q_2^2 + q_3^2 + q_4^2}, |q_1| \right), \end{aligned}$$

where

- q_i denotes the i th element in quaternion \mathbf{q}
- $\Delta \mathbf{r}^{-1}$ denotes the inverse of the quaternion $\Delta \mathbf{r}$
- $\mathbf{q} \times \mathbf{r}$ here denotes element-wise multiplication of the quaternions \mathbf{q} and \mathbf{r}
- $\text{atan2}(\cdot)$ is the two-argument version of the arctangent function.

Including the quaternion angular distance term $\mathcal{L}_{\text{Ang}}(\cdot)$ in the loss function incentivizes the DNN to learn features that are relevant to the geometry between the camera image and the local depth map. Hence, it provides additional supervision to the DNN training as a multi-task objective [39], and is important for the stability and speed of the training process.

The maximum likelihood loss term $\mathcal{L}_{\text{MLE}}(\cdot)$ depends on both the position error $\Delta \mathbf{x}$ and log variance $\log \sigma^2$ outputs from the DNN. The loss function is analogous to the negative log-likelihood of the Gaussian distribution,

$$\mathcal{L}_{\text{MLE}}(\mathbf{x}^*, \Delta \mathbf{x}, \log \sigma^2) = \sum_{X=x,y,z} D_{\text{MLE}}(\Delta X^*, \Delta X, \log \sigma_X^2)$$

$$D_{\text{MLE}}(a^*, a, \log \sigma_a^2) = \frac{1}{2} \log \sigma_a^2 + \frac{(a - a^*)^2}{2e^{\log \sigma_a^2}}.$$

If the variance output from the DNN is small, the corresponding position error is penalized much more than the position error corresponding to a large variance value. Hence, the maximum likelihood loss term $\mathcal{L}_{\text{MLE}}(\cdot)$ incentivizes the DNN to output low variance only when the corresponding position error output has high confidence, and otherwise output a high variance value.

5.4 Training Procedure

We train the DNN using stochastic gradient descent. Directly optimizing via the maximum likelihood loss term $\mathcal{L}_{\text{MLE}}(\cdot)$ might suffer from instability caused by the interdependence between the position error $\Delta \mathbf{x}$ and variance $\log \sigma^2$ outputs [40]. Therefore, we employ the mean-variance split training strategy proposed in [40]: First, we set $(\alpha_{\text{Huber}} = 1, \alpha_{\text{MLE}} = 1, \alpha_{\text{Ang}} = 1)$ and only optimize the parameters of CMRNet till validation error stops decreasing. Next, we set $(\alpha_{\text{Huber}} = 0, \alpha_{\text{MLE}} = 1, \alpha_{\text{Ang}} = 0)$ and optimize the parameters of VarianceNet. We alternate between these two steps till validation loss stops decreasing. Our DNN is implemented using the PyTorch library [41] and takes advantage of the open-source implementation available for CMRNet [14] as well as the available pretrained weights for initialization. Similar to CMRNet, all the layers in our DNN use the leaky RELU activation function with a negative slope of 0.1. We train the DNN on using a single NVIDIA Tesla P40 GPU with a batch size of 32 and learning rate of 10^{-5} selected via grid search.

5.5 Candidate State Selection

To assess the uncertainty in the DNN-based position error estimation process as well as the uncertainty from environmental factors, we evaluate the DNN output at N_C candidate states $\{\mathbf{s}_t^1, \dots, \mathbf{s}_t^{N_C}\}$ in the neighborhood of the state estimate \mathbf{s}_t .

For selecting the candidate states $\{\mathbf{s}_t^1, \dots, \mathbf{s}_t^{N_C}\}$, we randomly generate multiple values of translation offset $\{\mathbf{t}^1, \dots, \mathbf{t}^{N_C}\}$ and rotation offset $\{\mathbf{r}^1, \dots, \mathbf{r}^{N_C}\}$ about the state estimate \mathbf{s}_t , where N_C is the total number of selected candidate states. The i th translation vector $\mathbf{t}^i \in \mathbb{R}^3$ denotes translation in x , y and z dimensions and is sampled from a uniform probability distribution between a specified range $\pm t_{\text{max}}$ in each dimension. Similarly, the i th rotation vector \mathbf{r}^i comprises of 3 elements denoting rotation in roll, pitch and yaw dimensions, and is sampled from a uniform probability distribution between $\pm r_{\text{max}}$ in each dimension. The i th candidate state \mathbf{s}_t^i is generated by rotating and translating the state estimate \mathbf{s}_t by \mathbf{r}^i and \mathbf{t}^i , respectively. Corresponding to each candidate state \mathbf{s}_t^i , we generate a local depth map $L(\mathbf{s}_t^i, \mathcal{M})$ using the procedure laid out in Section V.1.

5.6 Multiple Samples of State Estimate Position Error

Using each local depth map $L(\mathbf{s}_t^i, \mathcal{M})$ and camera image I_t for the i th candidate state \mathbf{s}_t^i as inputs to the DNN in Section V.2, we evaluate the candidate state position error $\Delta \mathbf{x}_t^i$ and variance $(\sigma_t^i)^2$. From the known translation offset \mathbf{t}^i between the candidate state \mathbf{s}_t^i and the state estimate \mathbf{s}_t , we compute the transformation matrix $H_{\mathbf{s}_t^i \rightarrow \mathbf{s}_t}$ for converting the reference frame from the candidate state \mathbf{s}_t^i to the state estimate \mathbf{s}_t ,

$$H_{\mathbf{s}_t^i \rightarrow \mathbf{s}_t} = \begin{bmatrix} I_{3 \times 3} & -\mathbf{t}^i \end{bmatrix}, \quad (6)$$

where $I_{3 \times 3}$ denotes the identity matrix. Note that the rotation offset \mathbf{r}^i is not used in the transformation, since we are only concerned with the position errors from the true state \mathbf{s}_t^* to the state estimate \mathbf{s}_t , which are invariant to the orientation of the state estimate \mathbf{s}_t . Using the transformation matrix $H_{\mathbf{s}_t^i \rightarrow \mathbf{s}_t}$, we obtain the i th sample of the state estimate position error $\Delta \mathbf{x}_t^{(i)}$,

$$\Delta \mathbf{x}_t^{(i)} = H_{\mathbf{s}_t^i \rightarrow \mathbf{s}_t} \cdot [\Delta \mathbf{x}_t^i \quad 1]^\top. \quad (7)$$

The samples of state estimate position error $\{\Delta \mathbf{x}_t^{(1)}, \dots, \Delta \mathbf{x}_t^{(N_C)}\}$ represent both inaccuracy in the DNN estimation as well as uncertainties due to environmental factors. If the DNN approximation fails at the input corresponding to the state estimate \mathbf{s}_t , the estimated position errors at candidate states would lead to a wide range of different values for the state estimate position errors. Similarly, if the environment map \mathcal{M} near the state estimate \mathbf{s}_t contains repetitive features, the position errors computed from candidate states would be different and hence indicate high uncertainty. Note that the variance $(\sigma_t^i)^2$ computed from candidate state \mathbf{s}_t^i need not be transformed, since the translation offset \mathbf{t}^i does not contain any stochastic elements.

5.7 Outlier Weights

Since the candidate states $\{\mathbf{s}_t^1, \dots, \mathbf{s}_t^{N_C}\}$ are selected randomly, some position error samples may correspond to the local depth map and camera image pairs for which the DNN performs poorly. Thus, we compute outlier weights $\{\mathbf{w}_t^{(1)}, \dots, \mathbf{w}_t^{(N_C)}\}$ corresponding to the position error samples $\{\Delta \mathbf{x}_t^{(1)}, \dots, \Delta \mathbf{x}_t^{(N_C)}\}$ to mitigate the effect of these erroneous position error values in determining the protection levels. We compute outlier weights in each of the x , y , and z -dimensions separately, since the DNN approximation might not necessarily fail in all of its outputs. For computing the outlier weights $\mathbf{w}_t^{(i)} = [w_{x,t}^{(i)}, w_{y,t}^{(i)}, w_{z,t}^{(i)}]$ associated with the i th position error value $\Delta \mathbf{x}_t^{(i)} = [\Delta x_t^{(i)}, \Delta y_t^{(i)}, \Delta z_t^{(i)}]$, we employ the robust Z-score based outlier detection technique [32]. The robust Z-score is used in a variety of anomaly detection approaches due to its resilience to outliers [42]. We apply the following operations in each dimension $X = x, y$, and z :

1. We compute the Median Absolute Deviation statistic [32] MAD_X using all position error values $\{\Delta X_t^{(1)}, \dots, \Delta X_t^{(N_C)}\}$,

$$MAD_X = \text{median}(|\Delta X_t^{(i)} - \text{median}(\Delta X_t^{(i)})|). \quad (8)$$

2. Using the statistic MAD_X , we compute the robust Z-score $\mathcal{Z}_X^{(i)}$ for each position error value $\Delta X_t^{(i)}$,

$$\mathcal{Z}_X^{(i)} = \frac{|\Delta X_t^{(i)} - \text{median}(\Delta X_t^{(i)})|}{MAD_X}. \quad (9)$$

The robust Z-score $\mathcal{Z}_X^{(i)}$ is high if the position error $\Delta \mathbf{x}^{(i)}$ deviates from the median error with a large value when compared with the median deviation value.

3. We compute the outlier weights $\{w_X^{(1)}, \dots, w_X^{(N_C)}\}$ from the robust Z-scores $\{\mathcal{Z}_X^{(1)}, \dots, \mathcal{Z}_X^{(N_C)}\}$ by applying the softmax operation [43] such that the sum of weights is unity,

$$w_{X,t}^{(i)} = \frac{e^{-\gamma \cdot \mathcal{Z}_X^{(i)}}}{\sum_{j=1}^{N_C} e^{-\gamma \cdot \mathcal{Z}_X^{(j)}}}, \quad (10)$$

where γ denotes the scaling coefficient in the softmax function. We set $\gamma = 0.6745$ as the approximate inverse of the standard normal distribution evaluated at $3/4$ to make the scaling in the statistic consistent with the standard deviation of a normal distribution [32]. A small value of outlier weight $w_{X,t}^{(i)}$ indicates that the position error $\Delta X_t^{(i)}$ is an outlier.

5.8 Projection of Position Errors in Error Direction

We robustly estimate the horizontal direction of position error using the x and y -dimension position error samples and weights. For vertical dimension errors, the analogous direction is the z -axis itself. For brevity, we represent the outlier weights $W_{x,t}^{N_C}, W_{y,t}^{N_C}, W_{z,t}^{N_C}$, position errors $E_{x,t}^{N_C}, E_{y,t}^{N_C}, E_{z,t}^{N_C}$ and associated variances $V_{x,t}^{N_C}, V_{y,t}^{N_C}, V_{z,t}^{N_C}$ as $N_C \times 1$

matrices,

$$\begin{aligned} W_{X,t}^{N_C} &= [w_{X,t}^{(1)} \quad \dots \quad w_{X,t}^{(N_C)}]^\top \\ E_{X,t}^{N_C} &= [\Delta X_t^{(1)} \quad \dots \quad \Delta X_t^{(N_C)}]^\top \\ V_{X,t}^{N_C} &= [(\sigma_{X,t}^2)^1 \quad \dots \quad (\sigma_{X,t}^2)^{N_C}]^\top, \end{aligned}$$

where $X = x, y,$ or z dimension. Using the outlier weights $W_{x,t}^{N_C}, W_{y,t}^{N_C}$ and position errors $E_{x,t}^{N_C}, E_{y,t}^{N_C}$, we compute the horizontal error direction θ_h ,

$$\theta_h = \text{atan2} \left(\left(W_{y,t}^{N_C} \right)^\top E_{y,t}^{N_C}, \left(W_{x,t}^{N_C} \right)^\top E_{x,t}^{N_C} \right). \quad (11)$$

Then, we project the position errors and variances in x and y dimensions to the horizontal error direction θ_h and compute the magnitudes,

$$\begin{aligned} E_{h,t}^{2N_C} &= \left[\left| (\cos \theta_h)^{-1} \cdot \left(E_{x,t}^{N_C} \right)^\top \right| \quad \left| (\sin \theta_h)^{-1} \cdot \left(E_{y,t}^{N_C} \right)^\top \right| \right]^\top \\ V_{h,t}^{2N_C} &= \left[\left| (\cos \theta_h)^{-2} \cdot \left(V_{x,t}^{N_C} \right)^\top \right| \quad \left| (\sin \theta_h)^{-2} \cdot \left(V_{y,t}^{N_C} \right)^\top \right| \right]^\top, \end{aligned}$$

where

- $E_{h,t}^{2N_C}$ denotes the $2N_C \times 1$ matrix of horizontal position error magnitudes with elements denoted as $\Delta h_t^{(i)}$
- $V_{h,t}^{2N_C}$ denotes the $2N_C \times 1$ matrix of horizontal position error variances with elements denoted as $(\sigma_{h,t}^2)^{(i)}$
- $|\cdot|$ denotes elementwise magnitude.

The corresponding outlier weights $w_{h,t}^{(i)} \in W_{h,t}^{2N_C}$ are computed from $W_{x,t}^{N_C}, W_{y,t}^{N_C}$ by normalizing them to have unity sum,

$$W_{h,t}^{2N_C} = \left[0.5 \cdot \left(W_{x,t}^{N_C} \right)^\top \quad 0.5 \cdot \left(W_{y,t}^{N_C} \right)^\top \right]^\top. \quad (12)$$

Here, we simplify the problem and assume that the DNN outputs in the x and y dimensions are independently estimated. This assumption might not necessarily hold, since a common set of features is used in the DNN to determine the position error in all dimensions. However, we reason that the DNN loss function $\mathcal{L}(\Delta \mathbf{x}^*, \Delta \mathbf{x}, \log \sigma^2)$ treats the position error in each of the dimensions independently, and hence the assumption of position error independence across dimensions is justified.

Since the vertical error direction is the z -axis itself, we simply obtain the vertical position error magnitudes $\Delta v_t^{(i)} \in E_{v,t}^{N_C}$, variances $(\sigma_{v,t}^2)^{(i)} \in V_{v,t}^{N_C}$ and outlier weights $w_{v,t}^{(i)} \in W_{v,t}^{N_C}$,

$$\begin{aligned} E_{v,t}^{N_C} &= |E_{z,t}^{N_C}| \\ V_{v,t}^{N_C} &= V_{z,t}^{N_C} \\ W_{v,t}^{N_C} &= W_{z,t}^{N_C}. \end{aligned}$$

Note that the horizontal position error magnitudes $E_{h,t}^{2N_C}$ have twice the number of elements as compared with vertical error magnitudes $E_{v,t}^{N_C}$, since the horizontal errors incorporate both x and y dimension outputs from the DNN.

5.9 Probability Distribution of Position Error Magnitude

We construct a probability distribution in each of the horizontal and vertical dimensions from the previously obtained samples of position error magnitudes $E_{h,t}^{2N_C}, E_{v,t}^{N_C}$, variances $V_{h,t}^{2N_C}, V_{v,t}^{N_C}$ and outlier weights $W_{h,t}^{2N_C}, W_{v,t}^{N_C}$. We model the probability distribution using the Gaussian Mixture Model (GMM) distribution [33],

$$\begin{aligned} \mathbb{P}(h_t) &= \sum_{i=1}^{2N_C} w_{h,t}^{(i)} \mathcal{N} \left(\Delta h_t^{(i)}, (\sigma_{h,t}^2)^{(i)} \right) \\ \mathbb{P}(v_t) &= \sum_{i=1}^{N_C} w_{v,t}^{(i)} \mathcal{N} \left(\Delta v_t^{(i)}, (\sigma_{v,t}^2)^{(i)} \right), \end{aligned}$$

where

- h_t, v_t are the random variables for the horizontal position error magnitude and vertical position error magnitude at time t , respectively
- $\mathcal{N}(\mu, \sigma^2)$ is the Gaussian distribution with mean μ and variance σ^2 .

The probability distributions $\Pr(h_t)$ and $\Pr(v_t)$ incorporate both aleatoric uncertainty from the DNN-based variances and epistemic uncertainty from the multiple DNN evaluations associated with different candidate states. The epistemic uncertainty is reflected in the multiple GMM components and their weight coefficients, which represent the different possible position error values that may arise from the same camera image measurement and the environment map. The aleatoric uncertainty is present as the variance in each possible value of the position error represented by the individual components.

5.10 Protection Levels

We compute the protection levels using the probability distributions associated with horizontal and vertical directions. First, we obtain the cumulative distribution function $\text{CDF}(\cdot)$ for each probability distribution,

$$\begin{aligned} \text{CDF}(h_t) &= \sum_{i=1}^{2N_C} w_{h,t}^{(i)} \Phi \left(\frac{h_t - \Delta h_t^{(i)}}{(\sigma_{h,t}^2)^{(i)}} \right) \\ \text{CDF}(v_t) &= \sum_{i=1}^{N_C} w_{v,t}^{(i)} \Phi \left(\frac{v_t - \Delta v_t^{(i)}}{(\sigma_{v,t}^2)^{(i)}} \right), \end{aligned}$$

where $\Phi(\cdot)$ is the cumulative distribution function of the standard normal distribution. Then, for a specified value of the integrity risk IR , we compute the protection level PL in horizontal and vertical directions by employing a simple interval halving method for line search or the bisection method [44],

$$PL_{X,t} = \sup\{X_t : \text{CDF}(X_t) \leq 1 - IR\},$$

where $X = h$ or v . We specify an upper limit on the size of the protection level of 5 m that is larger than the maximum translation error that is considered in training the DNN.

The computed protection levels consider heavy-tails in the GMM probability distribution of the position error magnitude that arise because of the different possible values of the position error that can be computed from the available camera measurements and environment map. Our method computes large protection levels when many different values of position error may be equally probable from the measurements, resulting in larger tail probabilities in the GMM, and small protection levels only if the uncertainty from both aleatoric and epistemic sources is small.

6 Experimental Results

6.1 Real-World Driving Dataset

We use the KITTI visual odometry dataset [45] to evaluate the performance of the protection levels computed by our approach. The dataset was recorded around Karlsruhe, Germany over multiple driving sequences and contains images recorded by multiple on-board cameras, along with ground truth positions and orientations. Additionally, the dataset contains LiDAR point cloud measurements which we use to generate the environment map corresponding to each sequence. Since our approach for computing protection levels just requires a monocular camera sensor, we use the images recorded by the left RGB camera in our experiments. We use the sequences 00, 03, 05, 06, 07, 08 and 09 from the dataset based on the availability of a LiDAR environment map. We use sequence 00 for validation of our approach and the rest of the sequences are utilized in training our DNN. The experimental parameters are provided in Table 1.

6.2 LiDAR Environment Map

To construct a precise LiDAR map \mathcal{M} of the environment, we exploit the openly available position and orientation values for the dataset computed via Simultaneous Localization and Mapping [11]. Similar to [14], we aggregate the LiDAR point clouds across all time instances using the Open3D library [46]. Then, we detect and remove sparse outliers within the aggregated point cloud by computing Z-score [32] of each point in a 0.1 m local neighborhood. We

Parameter	Value
Integrity risk IR	0.01
Maximum PL size	5 m
Candidate state maximum translation offset t_{max}	1.5 m
Candidate state maximum rotation offset r_{max}	5°
Number of candidate states	32
Alarm limit	1.8 m

Table 1: Table of experimental parameters

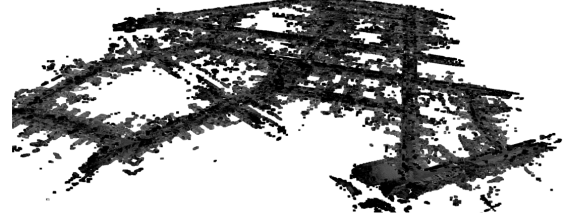


Figure 4: 3D LiDAR environment map from KITTI dataset sequence 00 [45].

discarded the points which had a higher Z-score than 3. Finally, the remaining points are down sampled using the Open3D library into a voxel map of the environment \mathcal{M} with resolution of 0.1 m. The corresponding map for sequence 00 in the KITTI dataset is shown in Fig. 4. For storing large maps, we divide the LiDAR point cloud sequences into multiple overlapping parts and construct separate maps of roughly 500 Megabytes each.

6.3 DNN Training and Testing Datasets

We generate the training dataset for our DNN in two steps. First, we randomly select a state estimate s_t at time t from within a 2 m translation and a 10° rotation of the ground truth positions and orientations in each driving sequence. The translation and rotation used for generating the state estimate is utilized as the ground truth position error $\Delta \mathbf{x}_t^*$ and orientation error $\Delta \mathbf{r}_t^*$. Then, using the LiDAR map \mathcal{M} , we generate the local depth map $L(s_t, \mathcal{M})$ corresponding to the state estimate s_t and use it as the DNN input along with the camera image I_t from the driving sequence data. The training dataset comprises of camera images from 11455 different time instances, with the state estimate selected at runtime so as to have different state estimates for the same camera images in different epochs.

Similar to the data augmentation techniques described in [14], we

1. Randomly change contrast, saturation and brightness of images,
2. Apply random rotations in the range of $\pm 5^\circ$ to both the camera images and local depth maps,
3. Horizontally mirror the camera image and compute the local depth map using a modified camera projection matrix.

All three of these data augmentation techniques are used in training CMRNet in the first half of the optimization process. However, for training VarianceNet, we skip the contrast, saturation and brightness changes during the second half of the optimization so that the DNN can learn real-world noise features from camera images.

We generate the validation and test datasets from sequence 00 in the KITTI odometry dataset, which is not used for training. We follow a similar procedure as the one for generating the training dataset, except we do not augment the data. The validation dataset comprises of randomly selected 100 time instances from sequence 00, while the test dataset contains the remaining 4441 time instances in sequence 00.

6.4 Metrics

We evaluate the horizontal and vertical protection levels computed using our approach using the following three metrics (with subscript t dropped for brevity):

1. **Bound gap** measures the difference between the computed protection levels PL_h, PL_v and the true position error magnitude,

$$BG_h = \text{avg} \left(PL_h - \sqrt{(\Delta x^*)^2 + (\Delta y^*)^2} \right)$$

$$BG_v = \text{avg}(PL_v - |\Delta z^*|),$$

where

- BG_h and BG_v denote bound gaps in horizontal and vertical dimensions respectively
- $\text{avg}(\cdot)$ denotes the average computed over the test dataset for which the value of protection level is available and greater than position error

A small bound gap value BG_h, BG_v is desirable since a bound gap of 0 implies that the algorithm exactly estimates the position error magnitude with no uncertainty.

2. **Failure rate** measures the total fraction of time instances in the test data sequence for which the computed protection levels PL_h, PL_v are smaller than the true position error magnitude,

$$FR_h = \frac{1}{T_{\max}} \sum_{t=1}^{T_{\max}} \mathbb{1}_t \left(PL_h < \sqrt{(\Delta x^*)^2 + (\Delta y^*)^2} \right)$$

$$FR_v = \frac{1}{T_{\max}} \sum_{t=1}^{T_{\max}} \mathbb{1}_t (PL_v < |\Delta z^*|),$$

where

- FR_h and FR_v denote failure rates for horizontal and vertical protection levels, respectively
- $\mathbb{1}_t(\cdot)$ denotes the indicator function computed using the protection level and true position error values at time t . The indicator function evaluates to 1 if the event in its argument holds true, and otherwise evaluates to 0
- T_{\max} denotes the total time duration of the test sequence

The failure rate FR_h, FR_v should be consistent with the specified value of the integrity risk IR to meet the safety requirements.

3. **False alarm rate** is computed for a specified alarm limit AL_h, AL_v in the horizontal and vertical directions and measures the fraction of time instances in the test data sequence for which the computed protection levels PL_h, PL_v exceed the alarm limit AL_h, AL_v while the position error magnitude is within the alarm limits. We first define the following integrity events,

$$\Omega_{HPL} = (PL_h > AL_h)$$

$$\Omega_{HPE} = \left(\sqrt{(\Delta x^*)^2 + (\Delta y^*)^2} > AL_h \right)$$

$$\Omega_{VPL} = (PL_v > AL_v)$$

$$\Omega_{VPE} = (|\Delta z^*| > AL_v).$$

The complement of each event is denoted by $\bar{\Omega}_{HPL}, \bar{\Omega}_{HPE}, \bar{\Omega}_{VPL}, \bar{\Omega}_{VPE}$, respectively. Next, we define the counts for false alarms $N_{HF A}, N_{VF A}$, true alarms $N_{HT A}, N_{VT A}$ and the number of times the position error exceeds the alarm limit (system unavailable) N_{HPE}, N_{VPE} ,

$$N_{HF A} = \sum_{t=1}^{T_{\max}} \mathbb{1}_t (\Omega_{HPL} \cap \bar{\Omega}_{HPE}) \quad N_{VF A} = \sum_{t=1}^{T_{\max}} \mathbb{1}_t (\Omega_{VPL} \cap \bar{\Omega}_{VPE})$$

$$N_{HT A} = \sum_{t=1}^{T_{\max}} \mathbb{1}_t (\Omega_{HPL} \cap \Omega_{HPE}) \quad N_{VT A} = \sum_{t=1}^{T_{\max}} \mathbb{1}_t (\Omega_{VPL} \cap \Omega_{VPE})$$

$$N_{HPE} = \sum_{t=1}^{T_{\max}} \mathbb{1}_t (\Omega_{HPE}) \quad N_{VPE} = \sum_{t=1}^{T_{\max}} \mathbb{1}_t (\Omega_{VPE}).$$

Finally, we compute the false alarm rates FAR_h, FAR_v after normalizing the total number of position error magnitudes lying above and below the alarm limit AL ,

$$FAR_h = \frac{N_{HF A} \cdot (T_{\max} - N_{HPE})}{N_{HF A} \cdot (T_{\max} - N_{HPE}) + N_{HT A} \cdot N_{HPE}}$$

$$FAR_v = \frac{N_{VF A} \cdot (T_{\max} - N_{VPE})}{N_{VF A} \cdot (T_{\max} - N_{VPE}) + N_{VT A} \cdot N_{VPE}}.$$

6.5 Results

Fig. 5 shows the horizontal protection levels computed by our approach on randomly selected subsets of the test sequence. For clarity, protection levels are computed at every 5th time instance. Similarly, Fig. 6 shows the vertical

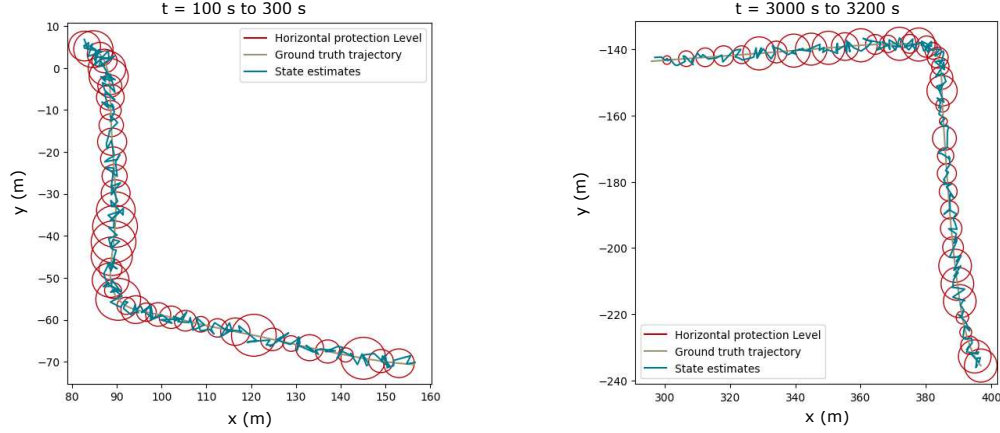


Figure 5: Horizontal protection level results on the test sequence in real-world dataset. We show protection levels for two subsets of the total sequence, computed at every 5 s intervals. The protection levels successfully enclose the position errors in a majority of the state estimates.

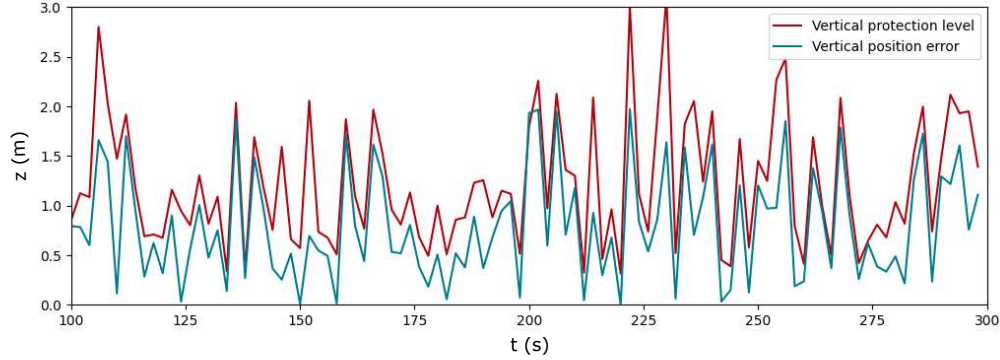


Figure 6: Vertical protection level results on the test sequence in real-world dataset. We show protection levels for a subset of the total sequence. The protection levels successfully enclose a majority of the position error magnitudes with a small bound gap.

protection levels along with the vertical position error magnitude in a subset of the test sequence. As can be seen from both the figures, the computed protection levels successfully enclose the position error magnitudes at a majority of the points in the visualized subsequences. Furthermore, the vertical protection levels are observed to be visually closer to the position error as compared to the horizontal protection levels. This is due to the superior performance of the DNN in determining position errors in the z -dimension, which is easier to learn since all the camera images in the dataset are captured by a ground-based vehicle.

Fig. 7 displays the integrity diagrams generated after the Stanford-ESA integrity diagram proposed for SBAS integrity [47]. The diagram is generated from 4441 samples of horizontal and vertical protection levels corresponding to different state estimates and camera images within the test sequence. Both the horizontal and vertical protection levels are greater than the position error magnitudes in about 99% cases. Note that the distribution of points along the position error axis in the two plots is different, because horizontal position errors in the test dataset depend on state estimate errors in both x and y dimensions, while the vertical position errors only depend on the z dimension state estimate errors.

We conducted an ablation study to numerically evaluate the impact of our proposed epistemic uncertainty measure and outlier weighting method in computing protection levels. We evaluated protection levels in three different cases: Incorporating DNN variance, epistemic uncertainty and outlier weighting (VAR+EO); incorporating just the DNN variance and epistemic uncertainty with equal weights assigned to all position error samples (VAR+E); and only using the DNN variance (VAR). For VAR, we constructed a Gaussian distribution using the DNN position error output and variance in each dimension. Then, we computed protection levels from the inverse cumulative distribution function of the Gaussian distribution corresponding to the specified value of integrity risk IR . Table 2 summarizes our results.

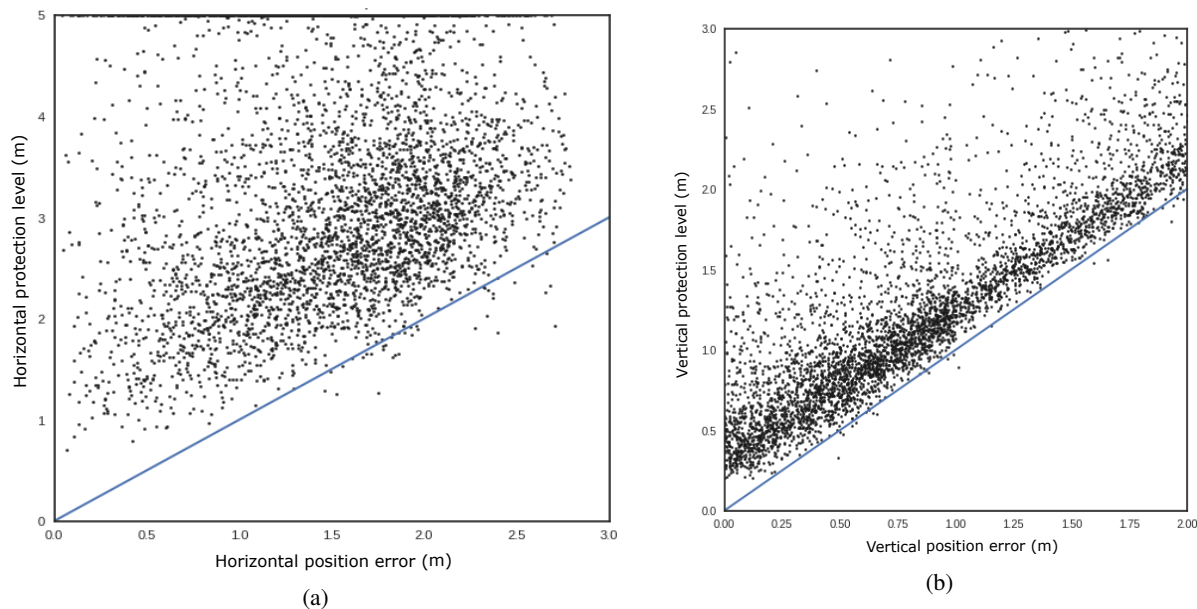


Figure 7: Integrity diagram results for the a) horizontal and b) vertical protection levels. The diagram contains protection levels evaluated across 4441 different state estimates and camera images from the test sequence. A majority of the samples are close to and greater than the position error magnitude, validating the applicability of the computed protection levels as a robust safety measure.

Incorporating the epistemic uncertainty in computing protection levels improved the failure rate from 0.09 in horizontal protection levels and 0.33 in vertical protection levels to about 0.01 in both cases. This is because the variance estimate from the DNN provides an overconfident measure of uncertainty, which is corrected by our epistemic uncertainty measure. Furthermore, incorporating outlier weighting reduced the bound gap by about 0.23 m in horizontal protection levels and 0.15 m in vertical protection levels as well as smaller false alarm rate while keeping the failure rate within the specified integrity risk requirement.

In horizontal dimension, the mean bound gap between the protection levels computed from our approach and the position error magnitudes is smaller than half the width of a standard U.S. lane. The corresponding value in the vertical dimension is even smaller, owing to the DNNs superior performance in determining position errors and uncertainty in the vertical dimension. This demonstrates the applicability of our approach to urban roads.

For an integrity risk requirement of 0.01, the protection levels computed by our method demonstrate a failure rate equal to or within 0.01 as well. However, further lowering the integrity risk requirement during our experiments either did not similarly improve the failure rate or caused a significant increase in the bound gaps. A possible reason is that the uncertainty approximated by our approach through both the aleatoric and epistemic measures fails to act as an accurate uncertainty representation for smaller integrity risk requirements than 0.01. Future research would consider more training data, better techniques for selecting candidate states, as well as different DNN architectures to meet smaller integrity risk requirements.

7 Conclusions

In this work, we presented a data-driven approach for computing horizontal and vertical protection levels associated with a given state estimate from camera images and a 3D LiDAR map of the environment. Our approach estimates both aleatoric and epistemic measures of uncertainty for computing protection levels, thereby providing robust measures of localization safety. We demonstrated the efficacy of our method on real-world data in terms of bound gap, failure rate and false alarm rate. Results show that the horizontal and vertical protection levels computed from our method enclose the position error magnitudes with 0.01 probability of failure and less than 1.6 m bound gap, which demonstrates that our approach is applicable to GNSS-denied urban environments.

	Horizontal PL			Vertical PL		
	$BG(m)$	FR	FAR	$BG(m)$	FR	FAR
VAR+EO	1.42	0.01	0.47	0.41	<0.01	0.28
VAR+E	1.65	<0.01	0.49	0.56	≈ 0.00	0.33
VAR	0.68	0.09	0.37	0.15	0.33	0.09

Table 2: Evaluation of horizontal and vertical protection levels from our approach. We compare protection levels computed by our best performing model using DNN variance, epistemic uncertainty and outlier weighting (VAR+EO), DNN variance and epistemic uncertainty (VAR+E) and only DNN variance (VAR) epistemic uncertainty. Incorporating epistemic uncertainty results in lower failure rate, while incorporating outlier weights reduces bound gap and false alarm rate.

Acknowledgements

This material is based upon work supported by the National Science Foundation under award #2006162.

References

- [1] Ryan W Wolcott and Ryan M Eustice. Robust LIDAR localization using multiresolution Gaussian mixture maps for autonomous driving. *The International Journal of Robotics Research*, 36(3):292–319, 2017.
- [2] Anirudh Viswanathan, Bernardo R Pires, and Daniel Huber. Vision-based robot localization across seasons and in remote locations. In *2016 IEEE International Conference on Robotics and Automation (ICRA)*, pages 4815–4821. IEEE, 2016.
- [3] Morten Bornø Jensen, Mark Philip Philipsen, Andreas Møgelmoose, Thomas Baltzer Moeslund, and Mohan Manubhai Trivedi. Vision for looking at traffic lights: Issues, survey, and perspectives. *IEEE Transactions on Intelligent Transportation Systems*, 17(7):1800–1815, 2016.
- [4] Daniel Dellinger, Andrew V Goldberg, Thomas Pajor, and Renato F Werneck. Customizable route planning in road networks. *Transportation Science*, 51(2):566–591, 2017.
- [5] Pratap Misra and Per Enge. Global Positioning System: signals, measurements and performance second edition.
- [6] Yiping Jiang and Jinling Wang. A new approach to calculate the horizontal protection level. *The Journal of Navigation*, 69(1):57–74, 2016.
- [7] Miguel Azaola et al. Isotropy-Based Protection Levels: a Novel Method for Autonomous Protection Level Computation with Minimum Assumptions, 2008.
- [8] Hieu Trung Tran and Letizia Lo Presti. Kalman filter-based ARAIM algorithm for integrity monitoring in urban environment.
- [9] Claudine Badue, Rânik Guidolini, Raphael Vivacqua Carneiro, Pedro Azevedo, Vinicius Brito Cardoso, Avelino Forechi, Luan Jesus, Rodrigo Berriel, Thiago Meireles Paixão, Filipe Mutz, et al. Self-driving cars: A survey. *Expert Systems with Applications*, page 113816, 2020.
- [10] Marcus A Brubaker, Andreas Geiger, and Raquel Urtasun. Map-based probabilistic visual self-localization. *IEEE transactions on pattern analysis and machine intelligence*, 38(4):652–665, 2015.
- [11] Tim Caselitz, Bastian Steder, Michael Ruhnke, and Wolfram Burgard. Monocular camera localization in 3d lidar maps. In *2016 IEEE/RSJ International Conference on Intelligent Robots and Systems (IROS)*, pages 1926–1931. IEEE, 2016.
- [12] Lauro J Lyrio, Thiago Oliveira-Santos, Claudine Badue, and Alberto Ferreira De Souza. Image-based mapping, global localization and position tracking using VG-RAM weightless neural networks. In *2015 IEEE International Conference on Robotics and Automation (ICRA)*, pages 3603–3610. IEEE, 2015.
- [13] Gabriel L Oliveira, Noha Radwan, Wolfram Burgard, and Thomas Brox. Topometric localization with deep learning. In *Robotics Research*, pages 505–520. Springer, 2020.
- [14] Daniele Cattaneo, Matteo Vaghi, Augusto Luis Ballardini, Simone Fontana, Domenico G Sorrenti, and Wolfram Burgard. Cmrnet: Camera to lidar-map registration. In *2019 IEEE Intelligent Transportation Systems Conference (ITSC)*, pages 1283–1289. IEEE, 2019.

- [15] Daniele Cattaneo, Domenico Giorgio Sorrenti, and Abhinav Valada. CMRNet++: Map and Camera Agnostic Monocular Visual Localization in LiDAR Maps. *arXiv preprint arXiv:2004.13795*, 2020.
- [16] Paul-Edouard Sarlin, Cesar Cadena, Roland Siegwart, and Marcin Dymczyk. From coarse to fine: Robust hierarchical localization at large scale. In *Proceedings of the IEEE Conference on Computer Vision and Pattern Recognition*, pages 12716–12725, 2019.
- [17] Hajime Taira, Masatoshi Okutomi, Torsten Sattler, Mircea Cimpoi, Marc Pollefeys, Josef Sivic, Tomas Pajdla, and Akihiko Torii. InLoc: Indoor visual localization with dense matching and view synthesis. In *Proceedings of the IEEE Conference on Computer Vision and Pattern Recognition*, pages 7199–7209, 2018.
- [18] Benjamin Recht, Rebecca Roelofs, Ludwig Schmidt, and Vaishaal Shankar. Do imagenet classifiers generalize to imagenet? *arXiv preprint arXiv:1902.10811*, 2019.
- [19] Alex Kendall and Yarin Gal. What uncertainties do we need in bayesian deep learning for computer vision? In *Advances in neural information processing systems*, pages 5574–5584, 2017.
- [20] Antonio Loquercio, Mattia Segu, and Davide Scaramuzza. A general framework for uncertainty estimation in deep learning. *IEEE Robotics and Automation Letters*, 5(2):3153–3160, 2020.
- [21] Armen Der Kiureghian and Ove Ditlevsen. Aleatory or epistemic? Does it matter? *Structural safety*, 31(2): 105–112, 2009.
- [22] Rowan McAllister, Yarin Gal, Alex Kendall, Mark Van Der Wilk, Amar Shah, Roberto Cipolla, and Adrian Weller. Concrete problems for autonomous vehicle safety: Advantages of bayesian deep learning. International Joint Conferences on Artificial Intelligence, Inc., 2017.
- [23] Nan Yang, Lukas von Stumberg, Rui Wang, and Daniel Cremers. D3VO: Deep Depth, Deep Pose and Deep Uncertainty for Monocular Visual Odometry. In *Proceedings of the IEEE/CVF Conference on Computer Vision and Pattern Recognition*, pages 1281–1292, 2020.
- [24] Alex Kendall and Roberto Cipolla. Modelling uncertainty in deep learning for camera relocalization. In *2016 IEEE international conference on Robotics and Automation (ICRA)*, pages 4762–4769. IEEE, 2016.
- [25] Dropout as a bayesian approximation: Representing model uncertainty in deep learning, author=Gal, Yarin and Ghahramani, Zoubin. In *international conference on machine learning*, pages 1050–1059, 2016.
- [26] Charles Blundell, Julien Cornebise, Koray Kavukcuoglu, and Daan Wierstra. Weight uncertainty in neural networks. *arXiv preprint arXiv:1505.05424*, 2015.
- [27] Andrew YK Foong, David R Burt, Yingzhen Li, and Richard E Turner. Pathologies of factorised gaussian and mc dropout posteriors in bayesian neural networks. *stat*, 1050:2, 2019.
- [28] Shubh Gupta and Grace Xingxin Gao. Data-Driven Protection Levels for Camera and 3D Map-based Safe Urban Localization. In *Proceedings of the 33rd International Technical Meeting of the Satellite Division of The Institute of Navigation (ION GNSS+ 2020)*, St. Louis, MO, 2020.
- [29] Vicki Lukas and JM Stoker. 3D Elevation Program—Virtual USA in 3D. Technical report, US Geological Survey, 2016.
- [30] Sriram Krishnan, Christopher Crosby, Viswanath Nandigam, Minh Phan, Charles Cowart, Chaitanya Baru, and Ramon Arrowsmith. OpenTopography: a services oriented architecture for community access to LIDAR topography. In *Proceedings of the 2nd International Conference on Computing for Geospatial Research & Applications*, pages 1–8, 2011.
- [31] Cheng Wang, Chenglu Wen, Yudi Dai, Shangshu Yu, and Minghao Liu. Urban 3d modeling with mobile laser scanning: a review. *Virtual Reality & Intelligent Hardware*, 2(3):175–212, 2020.
- [32] Boris Iglewicz and David Caster Hoaglin. *How to detect and handle outliers*, volume 16. Asq Press, 1993.
- [33] Bruce G Lindsay. Mixture models: theory, geometry and applications. In *NSF-CBMS regional conference series in probability and statistics*, pages i–163. JSTOR, 1995.
- [34] Alex Kendall, Matthew Grimes, and Roberto Cipolla. Posenet: A convolutional network for real-time 6-dof camera relocalization. In *Proceedings of the IEEE international conference on computer vision*, pages 2938–2946, 2015.
- [35] Cesar Cadena, Luca Carlone, Henry Carrillo, Yasir Latif, Davide Scaramuzza, José Neira, Ian Reid, and John J Leonard. Past, present, and future of simultaneous localization and mapping: Toward the robust-perception age. *IEEE Transactions on robotics*, 32(6):1309–1332, 2016.

- [36] Ruggero Pintus, Enrico Gobbetti, and Marco Agus. Real-time rendering of massive unstructured raw point clouds using screen-space operators. In *Proceedings of the 12th International conference on Virtual Reality, Archaeology and Cultural Heritage*, pages 105–112, 2011.
- [37] Alexey Dosovitskiy, Philipp Fischer, Eddy Ilg, Philip Hausser, Caner Hazirbas, Vladimir Golkov, Patrick Van Der Smagt, Daniel Cremers, and Thomas Brox. FlowNet: Learning optical flow with convolutional networks. In *Proceedings of the IEEE international conference on computer vision*, pages 2758–2766, 2015.
- [38] Peter J Huber. Robust estimation of a location parameter. In *Breakthroughs in statistics*, pages 492–518. Springer, 1992.
- [39] Sebastian Ruder. An overview of multi-task learning in deep neural networks. *arXiv preprint arXiv:1706.05098*, 2017.
- [40] Nicki Skafté, Martin Jørgensen, and Søren Hauberg. Reliable training and estimation of variance networks. In *Advances in Neural Information Processing Systems*, pages 6326–6336, 2019.
- [41] Adam Paszke, Sam Gross, Francisco Massa, Adam Lerer, James Bradbury, Gregory Chanan, Trevor Killeen, Zeming Lin, Natalia Gimelshein, Luca Antiga, et al. Pytorch: An imperative style, high-performance deep learning library. In *Advances in neural information processing systems*, pages 8026–8037, 2019.
- [42] Peter J Rousseeuw and Mia Hubert. Anomaly detection by robust statistics. *Wiley Interdisciplinary Reviews: Data Mining and Knowledge Discovery*, 8(2):e1236, 2018.
- [43] Ian Goodfellow, Yoshua Bengio, Aaron Courville, and Yoshua Bengio. *Deep learning*, volume 1. MIT press Cambridge, 2016.
- [44] Richard L Burden and J Douglas Faires. 2.1 The bisection algorithm. *Numerical analysis*, pages 46–52, 1985.
- [45] Andreas Geiger, Philip Lenz, and Raquel Urtasun. Are we ready for autonomous driving? the kitti vision benchmark suite. In *2012 IEEE Conference on Computer Vision and Pattern Recognition*, pages 3354–3361. IEEE, 2012.
- [46] Qian-Yi Zhou, Jaesik Park, and Vladlen Koltun. Open3D: A modern library for 3D data processing. *arXiv preprint arXiv:1801.09847*, 2018.
- [47] M Tossaint, Jaron Samson, Felix Toran, Javier Ventura-Traveset, J Sanz, Manuel Hernandez-Pajares, and JM Juan. The Stanford–ESA Integrity Diagram: Focusing on SBAS Integrity.